A New Ordered Oxygen-Deficient Manganite Perovskite: $LaBaMn_2O_{5.5}$. Crystal and Magnetic Structure

V. Caignaert,* F. Millange, B. Domengès, and B. Raveau

Laboratoire CRISMAT, C.N.R.S. UMR 6508, ISMRA. B^d Maréchal Juin, 14050 CAEN Cedex, France

E. Suard

Institut Laue-Langevin, 38042 GRENOBLE Cedex 9, France

Received July 1, 1998. Revised Manuscript Received January 27, 1999

A new ordered oxygen-deficient perovskite, $LaBaMn_2O_{5.5}$, has been synthesized, using the topotactic deoxygenation of the ordered $LaBaMn_2O_6$ perovskite. The crystal structure of this manganite was solved in the space group *Ammm* ($a = 3.86$ Å, $b = 8.19$ Å, $c = 15.47$ Å) from neutron powder diffraction data. The $[Mn_2O_{5.5}]_\infty$ framework is build up of row of MnO_6 octahedra and MnO_5 pyramids running along $\vec{a}$. This structure is intermediate between that of the ordered $LaBaMn_2O_6$ perovskite and that of $LaBaMn_2O_5$: it consists of ordered barium and lanthanum layers stacked alternatively along $\vec{c}$, oxygen vacancies being located at the level of the La layers. The magnetic structure is original: manganese spins form ferromagnetic spin-ladders along the $\vec{b}$ axis that are antiferromagnetically coupled along the $\vec{a}$ and $\vec{c}$ axis. The HREM investigation shows the existence of 90° oriented domains and twinning phenomena.

1. Introduction

Manganese oxides with a perovskite structure have received considerable attention these last years owing to their ability to exhibit colossal magnetoresistance (CMR) properties.[1−3] The understanding of this phenomenon requires a systematic study of the relationships between the structure and magnetic properties of the manganese oxide perovskites. In this respect, the La−Ba−Mn−O system is of a great interest considering that the perovskites $La_{1-x}Ba_xMnO_3$ are characterized by T_c up to 362 K.[4−6] In this system, several kinds of perovskites of formula $La_{1-x}Ba_xMnO_3$ have been isolated for the lanthanum-rich compositions i.e., $x < 0.4$.[4−6] Recently, the compositions corresponding to $x = 0.5$ have been investigated.[7] Two stoichiometric perovskites, $LaBaMn_2O_6$,[7] and one ordered oxygen-deficient perovskite, $LaBaMn_2O_5$,[7] have been synthesized. One form of the stoichiometric perovskites $LaBaMn_2O_6$ is cubic, in agreement with the complete disordering of lanthanum and barium, whereas the second form exhibits a tetragonal symmetry, due to the ordering of lanthanum and barium forming layers. The ordered oxygen-deficient perovskite $LaBaMn_2O_5$ is an homeotype of $YBaFeCuO_5$,[8] forming double pyramidal manganese layers containing the Ba^{2+} cations, and interleaved with lanthanum layers. These results show that the oxygen deficiency and the ordering of oxygen vacancies are closely related to the ordering of lanthanum and barium in the structure. They suggest the possibility to synthesize other original ordered oxygen-deficient perovskites with different oxygen stoichiometry. In the present paper, we report on the synthesis, crystal, and magnetic structures of a new oxygen-deficient perovskite $LaBaMn_2O_{5.5}$, whose ordering of oxygen vacancies and antiferromagnetic ordering have never been observed to date in perovskite-related structures.

2. Experimental Section

X-ray powder diffraction data were recorded at room temperature with a Philips diffractometer using Cu Kα radiation and a graphite backscattering monochromator. Neutron experiments were carried out at the Laue-Langevin Institut (Grenoble, France), with the high-resolution powder diffractometer D2b, using a wavelength $\lambda = 1.5939$ Å, between 1.7 K and room temperature. Patterns were recorded by step scanning, with 0.05° increments in 2θ, over the angular range $0° < 2\theta < 162.5°$. The medium-resolution D1b diffractometer ($\lambda = 2.52$ Å) was used to collect patterns between 1.5 K and 210 K. The nuclear and magnetic structures were analyzed

* Corresponding author. E-mail: caignaert@crismat.ismra.fr. Phone: 02-31-45-26-32. FAX: 02−31−95−16−00.

(1) von Helmolt, R.; Wecker, J.; Holzapfel, B.; Schutz, L.; Sammer, K. *Phys. Rev. Lett.* **1993**, *71*, 2331.
(2) Jin, S.; Tiefel, T. H.; McCormack, Fastnacht, R. A.; Ramesh, R.; Chen, L. H. *Science* **1994**, *264*, 413.
(3) Chahara, K.; Ohno, T.; Kasai, M.; Kozono, Y. *Appl. Phys. Lett.* **1993**, *63*, 1990.
(4) Jonker, G. H.; Van Santen, J. H. *Physica* **1950**, *16*, 337; Jonker, G. H. *Physica* **1956**, *22*, 702.
(5) Radaelli, P. G.; Marezio, M.; Hwang, H. Y.; Cheong, S. W. *J. Solid State Chem.* **1996**, *122*, 444.
(6) Barnabé, A.; Millange, F.; Maignan, A.; Hervieu, M.; Raveau, B.; Van Tendeloo, G.; Laffez, P. *Chem. Mater.* **1998**, *10*, 252.
(7) Millange, F.; Caignaert, V.; Domengès, B.; Raveau, B.; Suard, E. *Chem. Mater.* **1998**, *10*, 1974.
(8) Caignaert, V.; Mirebeau, I.; Bourée, F.; Nguyen, N.; Ducouret, A.; Greneche, J−M.; Raveau, B. *J. Solid State Chem.* **1995**, *114*, 24; Mombru, A. W.; Christides, C.; Lappas, A.; Prassides, K.; Pissas, M.; Mitros, C.; Niarchos, D. *Inorg. Chem.* **1994**, *33*, 1255.

10.1021/cm980469h CCC: $18.00
Published on Web 03/11/1999

with the Rietveld method using the program Fullprof.[9] This software allows both the conventional Rietveld refinement and the whole pattern fitting by the Le Bail method. The coherent scattering lengths used were $b_{La} = 0.824\ 10^{-12}$ cm, $b_{Ba} = 0.525\ 10^{-12}$ cm, $b_{Mn} = -0.373\ 10^{-12}$ cm, and $b_O = 0.580\ 10^{-12}$ cm.[10] The background was interpolated and the peak shape was described by a pseudo-Voigt function.

The electron microscopy was performed on a JEM 200CX equipped with a tilting, rotating goniometer, which allows reciprocal space reconstruction. High-resolution work was performed on a TOPCON 2B electron transmission microscope, equipped with a double-tilt (±10°) goniometer and an objective lens with a spherical aberration constant of 0.4 mm. EDS analysis was also used to verify the homogeneity of the phase. High-resolution images were calculated using the multislice method of EMS package.

The thermogravimetric (TG) analysis was realized with a Setaram microbalance under an oxygen flow and a heating rate of 4 °C/min.

The magnetic susceptibility was measured with a SQUID between 4K and room temperature with an applied field of 100 G.

3. Topotactic Synthesis

The first aim of the present study was to synthesize an oxygen-deficient perovskite, intermediate between the ordered stoichiometric perovskite $LaBaMn_2O_6$ and the ordered oxygen-deficient perovskite $LaBaMn_2O_5$, which are both characterized by identical stacking of the lanthanum and barium layers. It rapidly appeared that such a structure could not be obtained by a direct synthesis from oxides, according to the nominal composition $\ll LaBaMn_2O_{5.5} \gg$, due to its metastability. Thus, a soft chemistry method, based on topotactic reaction, operating at low temperature around 600 °C, had to be used, starting from the ordered $\ll LaBa \gg$ phases $LaBaMn_2O_6$ or $LaBaMn_2O_5$. The oxidation of $LaBaMn_2O_5$ at low temperature was found to be extremely fast and difficult to control, so the ordered $LaBaMn_2O_6$ was always obtained without any intermediate. In contrast, the ordered $LaBaMn_2O_6$ perovskite could be reduced topotactically, leading to the ordered perovskite $LaBaMn_2O_{5.5}$, i.e., $La_2Ba_2Mn_4O_{11}$, without any change of the La/Ba ordering. Such a controlled deoxygenation was performed by heating the ordered $LaBaMn_2O_6$ perovskite at 600 °C for 48 h in an evacuated silica ampule in the presence of powdered Ti metal. About 2 g of $LaBaMn_2O_6$, contained in an alumina crucible, was introduced into the ampule with the adequate amount of powered Ti metal. The titanium is oxidized in accordance with the reaction

$$4LaBaMn_2O_6 + Ti \rightarrow 4LaBaMn_2O_{5.5} + TiO_2$$

This reduction of $LaBaMn_2O_6$ can also be performed, at the same temperature, with chips of zirconium−titanium alloy. At higher temperature, typically 800 °C, the reduction leads to the compound $LaBaMn_2O_5$.

The oxygen content of the sample was then determined by reoxidation under oxygen by TG analysis, heating at a rate of 4 °C/mn. The final oxidized product was assumed to be the ordered $LaBaMn_2O_6$ perovskite.

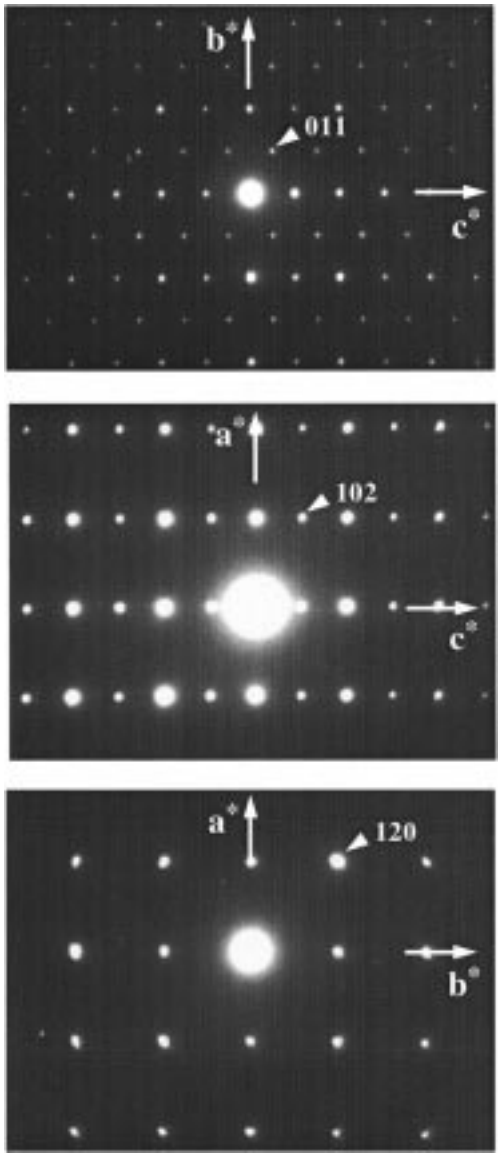

Figure 1. [100], [010] and [001] E. D. patterns showing existence conditions hkl, $k + l = 2n$. One should notice brighter spots related to a_p x a_p x $2a_p$ subcell.

This was confirmed from its powder X-ray diffraction pattern. Under these conditions, the weight gain, resulting from the oxidization of manganese, indicated that the composition of the so-obtained deficient perovskite was $LaBaMn_2O_{5.51\pm0.02}$, which leads to a trivalent state for the manganese cations. An important feature of this oxygen-deficient perovskite is its easy reoxidation at a temperature as low as 200 °C, which emphasizes the importance to ensure the storage of the sample in inert atmosphere. Moreover, the reversibility of this redox reaction shows the topotactic nature of the transformation between the ordered perovskite $LaBaMn_2O_6$ and the deficient perovskite $LaBaMn_2O_{5.5}$.

4. Nuclear and Magnetic Structure

4.1. Room Temperature Crystal Structure. To determine the cell parameters, an electron diffraction (ED) study was first performed on numerous microcrystals. The ED observations allow distinguishing, through their relative intensity, two sets of reflections, a strong one and a weaker one. The first one is related

(9) Rodriguez-Carvajal, J. in *Satellite Meeting on Powder Diffraction*, abstracts of the XVth Conference of the International Union of Crystallography (Toulouse, 1990), p 127.

(10) Sears, V. F. Chalk River Nuclear Lab. Internal report AECL-8490, 1984.

to $LaBaMn_2O_6$ double perovskite, indicating a $a_p \times a_p \times 2a_p$ subcell (Figure 1). The second one introduces a doubling of both $\vec{b}$ and $\vec{c}$ parameters, leading to the supercell $a_p \times 2a_p \times 4a_p$. Despite the frequent observation of 90° oriented domains inside microcrystals, the reconstruction of the reciprocal space could be performed and the existence of reflection conditions hkl, $k+l = 2n$ evidenced, compatible with an A centered cell. The space group $Ammm$ was chosen for the structure resolution.

The neutron powder diffraction data were analyzed first with a whole pattern-fitting algorithm in order to determine accurately the profile shape function, background, and cell parameters. This preliminary analysis has also the advantage of providing a good estimate of the R_{wp} and χ^2 that could be reached during the structure refinement. This whole pattern fitting led to $R_{wp} = 5.38\%$ and $\chi^2 = 1.25$. Small residual peaks remained which could not be indexed in the $LaBaMn_2O_{5.5}$ cell and were identified as MnO reflections. This impurity was present in the starting compound $LaBaMn_2O_6$. For the resolution of the oxygen-deficient structure of $LaBaMn_2O_{5.5}$, the two following features were considered:

(i) The cationic arrangement should be similar to that of the starting compound, due to the low temperature used during the reduction. Thus, the compound should have preserved the ordered stacking of the La and Ba layers.

(ii) The ordering of the oxygen vacancies, if it exists, follows the A centering, so that the $\vec{b}$ and $\vec{c}$ axis be doubled with respect to the cell parameters of the precursor $LaBaMn_2O_6$. This last requirement can be satisfied by an oxygen vacancy on the 2a site (0,0,0).

Thus, from the above considerations, the following ideal atomic parameters were used as starting positions for the refinement of the structure of $LaBaMn_2O_{5.5}$, in the space group

La	4j	1/2	0.25	0
Ba	4f	1/2	1/4	1/4
$Mn_{(1)}$	4g	0	0	0.125
$Mn_{(2)}$	4g	0	0	0.375
$O_{(1)}$	8p	0	0.25	0.125
$O_{(2)}$	4g	0	0	0.25
$O_{(3)}$	4h	1/2	0	0.125
$O_{(4)}$	4h	1/2	0	0.375
$O_{(5)}$	2b	0	0	1/2

The refinement was undertaken with the room-temperature neutron diffraction pattern for which the magnetic measurement showed a paramagnetic behavior. The refinement of the eight atomic positions and nine thermal parameters converged to give $R_{wp} = 6.11\%$, $R_p = 4.9\%$, $R_i = 5.66\%$, $\chi^2 = 1.59$. The use of noncentrosymmetric space groups does not decrease significantly the agreement factors. A refinement of partial oxygen occupancy of the 2a site gives 1% occupancy but with error bars greater than the occupancy itself. In the final refinement, this site is kept empty, which is in agreement with the stoichiometry determined by TG analysis and shows that there is no disorder on the anionic lattice. The refinement of La and Ba site occupancies shows that the 4j and 4f site are fully occupied by the La and Ba cations. Moreover, a statistical distribution (50% La, 50% Ba) on both sites leads to a higher reliability factor ($R_{wp} = 6.74\%$, $R_i = 7.16\%$, $\chi^2 = 1.98$) and irrealistic thermal factors ($B = -0.7$ Å^2 on 4j and $B = 1.7$ Å^2 on 4f). The weight fraction of the MnO impurity is about 1% of the sample mass, i.e., the same value that was refined in the precursor.[7] The observed, calculated, and difference profiles are plotted for the neutron (Figure 2) diffraction pattern. The final atomic coordinates are listed in Table 1, and interatomic distances are given in Table 2. Bond valence calculations for the cations (Table 2), using the parameters given by Brown[11] and the results of the NPD analysis, are in good agreement with the expected values.

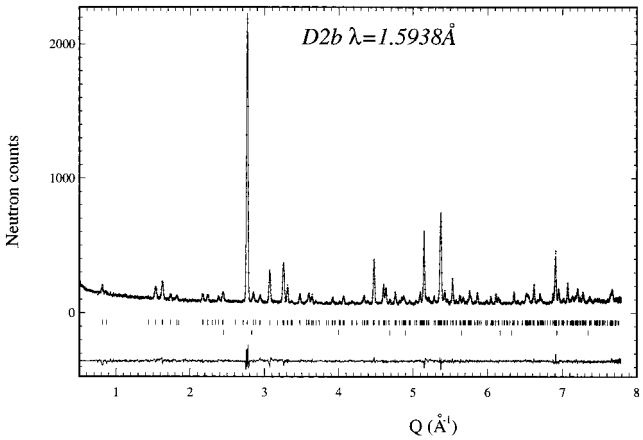

Figure 2. Rietveld refinement plot of neutron diffraction data. Observed, calculated, and difference profiles are plotted on the same scale. The Bragg peaks are indicated by tick marks (top, $LaBaMn_2O_{5.5}$; bottom: MnO).

Table 1. Structural Parameters for $LaBaMn_2O_{5.5}$ at Room Temperature and 1.7 K[a]

atom	site	position	RT	1.7 K	
La	4j	1/2 y 0	$y = 0.2670(7)$	0.2673(7)	
			$B = 0.15(4)$	0.19(6)	
Ba	4f	1/2 1/4 1/4	$B = 0.24(7)$	0.10(9)	
$Mn_{(1)}$	4g	0 0 z	$z = 0.1211(7)$	0.1182(7)	$\mu_y = 3.0(3)\ \mu_B$
			$B = 0.16(9)$	0.10(9)	
$Mn_{(2)}$	4g	0 0 z	$z = 0.3745(7)$	0.3737(7)	$\mu_y = 3.4(3)\ \mu_B$
			$B = 0.08(9)$	0.10(9)	
$O_{(1)}$	8p	0 y z	$y = 0.2297(6)$	0.2312(6)	
			$z = 0.1072(3)$	0.1077(3)	
			$B = 0.53(5)$	0.40(6)	
$O_{(2)}$	4g	0 0 z	$z = 0.2519(5)$	0.2516(5)	
			$B = 0.32(7)$	0.36(9)	
$O_{(3)}$	4h	1/2 0 z	$z = 0.0972(5)$	0.0960(5)	
			$B = 0.60(9)$	0.81(11)	
$O_{(4)}$	4h	1/2 0 z	$z = 0.3821(5)$	0.3827(5)	
			$B = 0.47(7)$	0.48(8)	
$O_{(5)}$	2b	0 0 1/2	$B = 0.31(11)$	0.10(13)	

[a] At room temperature: $a = 3.8564(2)$ Å, $b = 8.1883(4)$ Å, $c = 15.4734(8)$ Å. At 1.7 K: $a = 3.8445(2)$ Å, $b = 8.1849(4)$ Å, $c = 15.4258(8)$ Å.

The projection of the structure of $LaBaMn_2O_{5.5}$ along $\vec{a}$ is shown in Figure 3, where it is compared to the structure of the ordered stoichiometric perovskite $LaBaMn_2O_6$ and of the ordered deficient perovskite $LaBaMn_2O_5$. The structure of $LaBaMn_2O_{5.5}$ consists of two kinds of manganese polyhedra, MnO_5 pyramids labeled $Mn_{(1)}$ and MnO_6 octahedra labeled $Mn_{(2)}$, whereas one observes only MnO_6 octahedra in $LaBaMn_2O_6$ and only MnO_5 pyramids in $LaBaMn_2O_5$. Clearly, the struc-

(11) Brown, I. D.; Altermatt, D. *Acta Crystallogr. B* **1985**, *41*, 244; Hormillosa, C.; Healy S. Computer code VALENCE, McMaster University, Hamilton, Ontario, Canada, 1991.

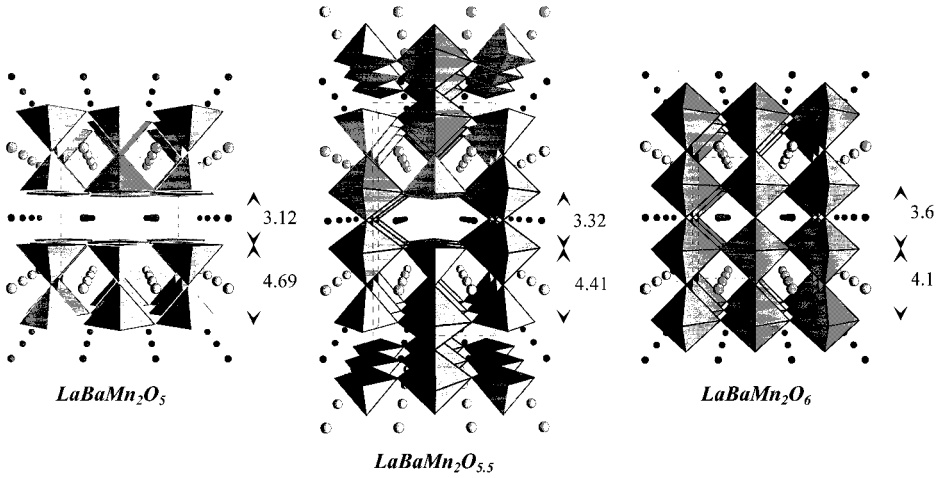

Figure 3. Perspective view of $LaBaMn_2O_5$, $LaBaMn_2O_{5.5}$, and $LaBaMn_2O_6$ structures. Mean oxygen−oxygen distances are given (Å).

Table 2. Interatomic Distance and Calculated Valence for $LaBaMn_2O_{5.5}$ at Room Temperature

bond	distance (Å)	multiplicity	valence
$La-O_{(1)}$	2.562(3)	×4	
$La-O_{(3)}$	2.654(7)	×2	2.96
$La-O_{(4)}$	2.640(7)	×2	
$La-O_{(5)}$	2.712(4)	×2	
$Ba-O_{(1)}$	2.938(3)	×4	
$La-O_{(2)}$	2.812(1)	×4	2.03
$La-O_{(3)}$	3.127(6)	×2	
$La-O_{(4)}$	2.893(6)	×2	
$Mn_{(1)}-O_{(1)}$	1.893(6)	×2	
$Mn_{(1)}-O_{(2)}$	2.025(14)	×1	3.04
$Mn_{(1)}-O_{(3)}$	1.963(3)	×2	
$Mn_{(2)}-O_{(1)}$	2.231(6)	×2	
$Mn_{(1)}-O_{(2)}$	1.898(14)	×1	3.12
$Mn_{(1)}-O_{(4)}$	1.932(1)	×2	
$Mn_{(1)}-O_{(5)}$	1.942(11)	×1	

ture of $LaBaMn_2O_{5.5}$ appears as intermediate between that of $LaBaMn_2O_6$ and that of $LaBaMn_2O_5$. It consists of rows of $Mn_{(1)}$ pyramids and of $Mn_{(2)}$ octahedra running along $\vec{a}$. Along $\vec{b}$, one octahedral row alternates with one pyramidal, whereas along $\vec{c}$, the chains of polyhedra are interrupted, due to the presence of oxygen vacancies, so that strings of four polyhedra are formed according to the sequence "$Mn_{(1)}-Mn_{(2)}-Mn_{(2)}-Mn_{(1)}$‥ ‥$Mn_{(1)}-Mn_{(2)}-Mn_{(2)}-Mn_{(1)}$". It results in the formation of flattened six-sided tunnels where the lanthanide cations are located. The similarity between the three structures is reinforced by the fact that they exhibit the same ordering of the La^{3+} and Ba^{2+} cations, forming layers parallel to (001). Along $\vec{c}$, one Ba layer alternates with one La layer, so that the geometry of the Mn polyhedra located at the level of those layers and especially the Mn−O distances are greatly influenced, due to the size difference between La^{3+} and Ba^{2+} cations. As a consequence, it is worth describing the three structures as a stacking of two different layers along $\vec{c}$, i.e., by the stacking of $LaMnO_3$ and $BaMnO_3$ layers for $LaBaMn_2O_6$, of $LaMnO_{2.5}$ and $BaMnO_3$ layers for $LaBaMn_2O_{5.5}$, and of $LaMnO_2$ and $BaMnO_3$ layers for $LaBaMn_2O_5$. The larger size of Ba^{2+} compared to La^{3+} means that the $BaMnO_3$ layers, characterized by the O−O distances or the Mn−Mn distances along $\vec{c}$ (Table 3), are significantly thicker than the $LaMnO_3$, $LaMnO_{2.5}$, or $LaMnO_2$ layers in the three structures. But at this point, a second important factor has to be considered to explain the structural evolution: the relaxation of the structure around the oxygen vacancies which are located in the lanthanum layers. Consequently, the thickness of these layers decreases as the oxygen content decreases, from 3.666 Å for $LaMnO_3$, to a mean value of 3.325 Å for $LaMnO_{2.5}$, and finally to 3.123 Å for $LaMnO_2$ (see Figure 3 and Table 3). In counterpart, the thickness of the $BaMnO_3$ layer increases from 4.130 Å for $LaBaMn_2O_6$, to a mean value of 4.419 Å for $LaBaMn_2O_{5.5}$, and finally to 4.690 Å for $LaBaMn_2O_5$. Keeping in mind these two factors, "La-Ba" size difference and oxygen vacancy relaxation effect, the direction of long Mn−O distances due to Jahn−Teller distortion of the Mn polyhedra in $LaBaMn_2O_{5.5}$ can be explained. The strain in the $LaMnO_{2.5}$ layer induces short $Mn_{(2)}-O_{(5)}$ distances along $\vec{c}$ in the $Mn_{(2)}$ octahedra (Table 2), while the extension in the $BaMnO_3$ will produce long apical $Mn_{(1)}-O_{(2)}$ distances along $\vec{c}$ in the $Mn_{(1)}$ pyramids (Table 2). Consequently the Jahn−Teller distortion of the $Mn_{(2)}$ octahedra can only extend along [010].

Table 3. Interatomic Distances along the $\vec{c}$ Axis (Perpendicular to Layers) for $LaBaMn_2O_5$, $LaBaMn_2O_{5.5}$, and $LaBaMn_2O_6$ at Room Temperature

		distance (Å)		
layer	bond	$LaBaMn_2O_5$	$LaBaMn_2O_{5.5}$	$LaBaMn_2O_6$
La	Mn−Mn	3.805	3.746	3.868
			3.883	
Ba	Mn−Mn	4.003	3.922	3.928
La	O−O	3.123	3.009	3.666
			3.317	
			3.649	
Ba	O−O	4.690	4.407	4.130
			4.432	

These results help to explain the magnetic structure of $LaBaMn_2O_{5.5}$, since they allow the orbital ordering of manganese to be deduced. They show indeed that the singlet occupied orbital (d_{z^2}) extends along [001] for $Mn_{(1)}$ in pyramidal coordination, whereas it is 90° oriented along [010] for $Mn_{(2)}$ in octahedral coordination. This peculiar orbital ordering is responsible for the magnetic structure that will be discussed further.

4.2. Microstructure. The microstructural study of the phase was performed by high-resolution transmission electron microscopy. To interpret the observed contrasts, simulated images were calculated for the

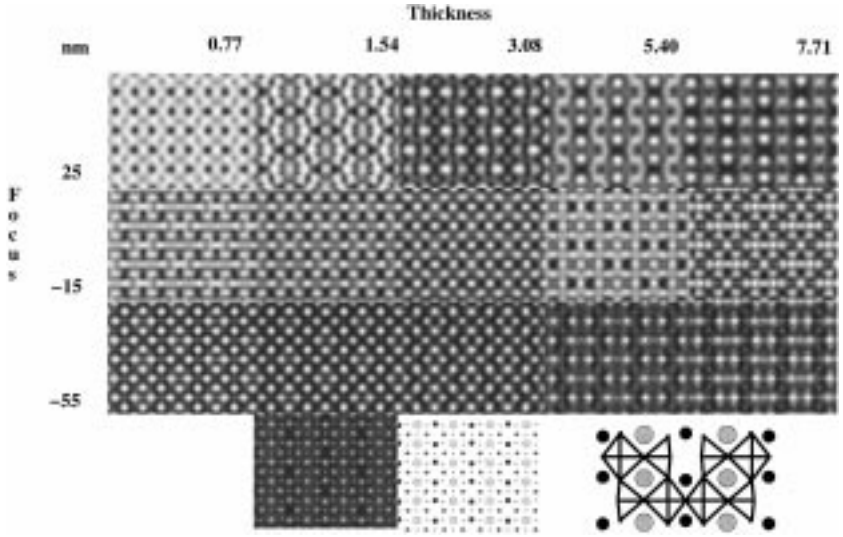

Figure 4. Typical [100] HREM images chosen in calculated through focus series for several crystal thicknesses. Projected potential and structure are joined.

[100] direction of observation, which is the most characteristic of the superstructure settlement. It appears that most focus values allow us to observe the superstructure, for thickness as low as 0.8 nm (Figure 4).

Most of the crystals show the fairly well-established superstructure $a_p \times 2a_p \times 4a_p$. Observed high-resolution [100] images confirm the A centering of the structure. Figure 5 show three characteristic experimental and calculated (inset) images. On the 25 nm focus image, the highest electron density zones are highlighted and brighter dots are related to lanthanum and barium cations. Also, oxygen vacancies and columns of oxygen atoms appear as black dots. Thus, the anionic framework neighboring the La and Ba cations affects the image contrast in such a way that it is very easy to distinguish them. Indeed, La cations appear as rows of bright dots following the sequence two bright dots, dark space, whereas Ba cations form zigzag rows of bright gray dots. On the −15 nm focus image, low electron density zones are highlighted. Oxygen and oxygen vacancies appear as bright dots, the brightest ones corresponding to the vacancies. Thus, parallel to the $\vec{c}$ direction, one can count one bright dot, three gray, one bright, and so on, the formed rows alternating along $\vec{b}$ in such a way to follow the A face centering. On −55 nm focus image, the intermediate electron density zones are highlighted and enhance the arrangement of the manganese atoms of the structure. Mn−O columns of the MnO_5 pyramids are imaged through bright dots slightly closer than those imaging the Mn−O columns of the MnO_6 octahedra, so that parallel to the $\vec{c}$ direction, two closer dots alternate with two spaced ones. Also barium columns appear as gray dots on the crystal edge. Though the contrast is very sensitive to crystal thickness, it could be verified that, most often, the superstructure is well-established and almost no defect affects its regularity.

A rather frequent phenomenon is the occurrence of 90° oriented domains. Indeed, the arithmetic relation between $\vec{a}$ and $\vec{c}$ parameters ($c/4a = 1.003$) and the framework a geometry associated to it allow an easy interchange of both directions. As an example, the microcrystal of Figure 6 is built up from several 90° oriented domains. The SAED pattern apparently corresponds to the classical [100] orientation, but one can notice that the spots which should be indexed as 0 2k 4l are stronger than usual. Furthermore, the SAED pattern taken with a shorter camera length lets the first-order Laue zone (FOLZ) appear, which shows an $1/a_p \times 1/a_p$ reciprocal lattice and is translated $1/2a_p$ parallely to b^*, in agreement with A face centering (hkl, $k + l = 2n$). Also, measuring the reciprocal diameter of FOLZ allows us to evaluate the reciprocal perpendicular parameter as close to $1/(4a_p)$, i.e., c^*. Thus, this ED pattern can be interpreted as the superimposition of two patterns identified as [100]- and [001]-type ones. Indeed, the corresponding HREM image shows several domains which can be distinguished through their contrast. The first type of contrast is characteristic of [100] images of $LaBaMn_2O_{5.5}$ structure, and the second type of contrast is perovskite like, but a rectangular deformation can be measured which is close to the $b/2a$ ratio. According to ED observations, this contrast can thus be interpreted as a [001] image of the $LaBaMn_2O_{5.5}$ structure. Details of the HREM image show that the domain boundary is most often parallel to the (012) plane (corresponding to $(011)_P$). It can easily be modalized through MnO_6 octahedra, ensuring the junction (Figure 7).

Twinning phenomena have also been encountered. They result from the building principle of the $LaBaMn_2O_{5.5}$ structure. The ED pattern of Figure 8 can be interpreted as a twinned microcrystal, the twinning plane being identified as (120), i.e., $(110)_p$ of the perovskite subcell. This means that the superstructure can take place along the two equivalent ⟨021⟩ directions of the perovskite subcell. The corresponding medium resolution image shows twinned domains as large as several tens of nanometers, and fringes perpendicular to the $[04\bar{1}]$ direction can be seen which image the change in the direction of superstructure settlement from one domain to the other. This twinning phenomenon can be easily modalized (Figure 9).

4.3. Magnetic Structure. The magnetic susceptibility measurements show an antiferromagnetic transition at a Neel temperature of $T_N \approx 185$ K. Below T_N, the temperature behavior of the $1/\chi$ curve is anomalous and

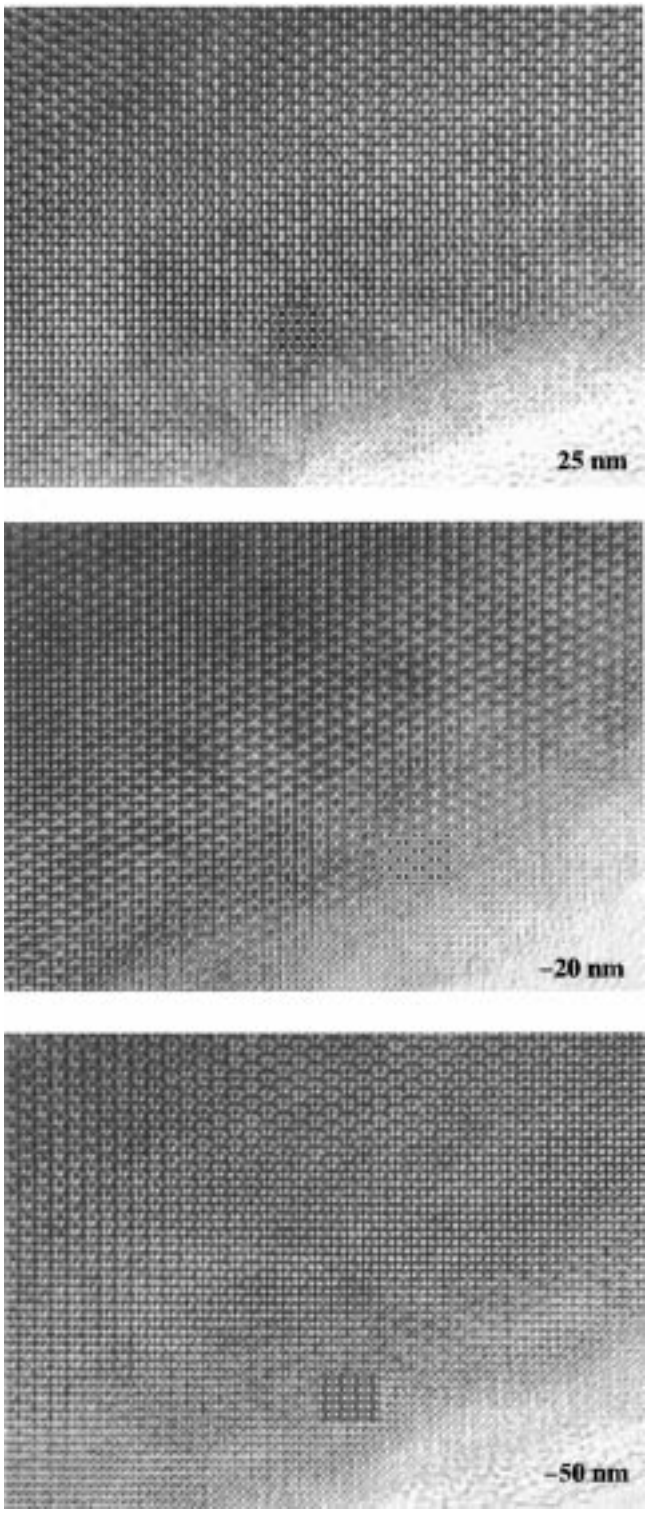

Figure 5. Three typical focus value [100] observed HREM images. Calculated images are inset; crystal thickness evaluated as close to 5 nm.

a second minimum is observed at $T \approx 90$ K. The neutron diffraction patterns (Figure 10), collected between 1.7 and 210 K, show that this cusp in the susceptibility coincides with the antiferromagnetic transition of MnO, which is detected as an impurity.

A comparison between low-temperature and room-temperature neutron diffraction data indicates the existence of several additional reflections at low temperature, which can be indexed on the basis of a

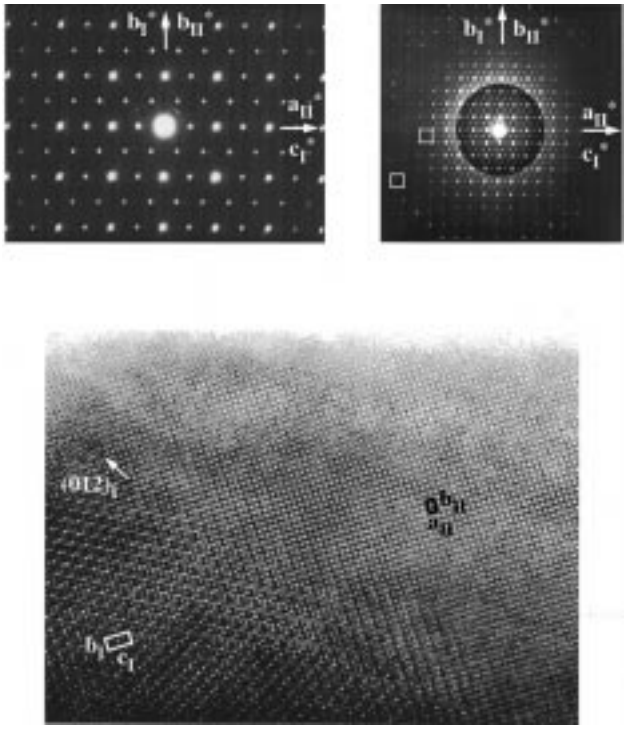

Figure 6. SAED pattern interpreted as the superimposition of two sets of dots (I and II), $hk0_{II}$ are superposed to $0k4h_I$. For the SAED pattern taken with a lower camera length, the set of dots of domain II is marqued through white squares on ZOLZ and FOLZ. The corresponding HREM image shows two domains.

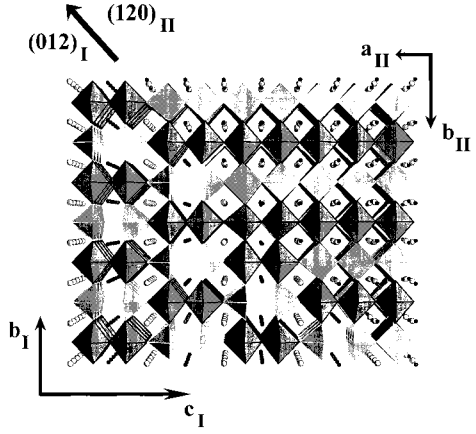

Figure 7. Proposed structural model for domain boundary observed in the previously mentioned crystal (MnO_6 octahedra and MnO_5 pyramids are dark gray and light gray shaded, respectively).

magnetic cell which is doubled along the $\vec{a}$ axis with respect to the nuclear cell, leading to a propagation vector of $\vec{k} = (1/2,0,0)$. Moreover the Miller indices of the magnetic reflections fulfill the parity rule $k + l = 2n + 1$.

The coupling modes of the magnetic moments in $LaBaMn_2O_{5.5}$, which are compatible with the crystal symmetry, have been determined for a propagation vector $\vec{k} = (0,0,0)$ using Bertaut's group theoretical method.[12] The inversion center $\bar{1}$ and the 2_{1y}, 2_{1z} screw axis were chosen as independent symmetry elements of the space group *Ammm* for the 4g positions of the

(12) Bertaut, E. F. *Acta Crystallogr.* **1968**, *A24*, 217.

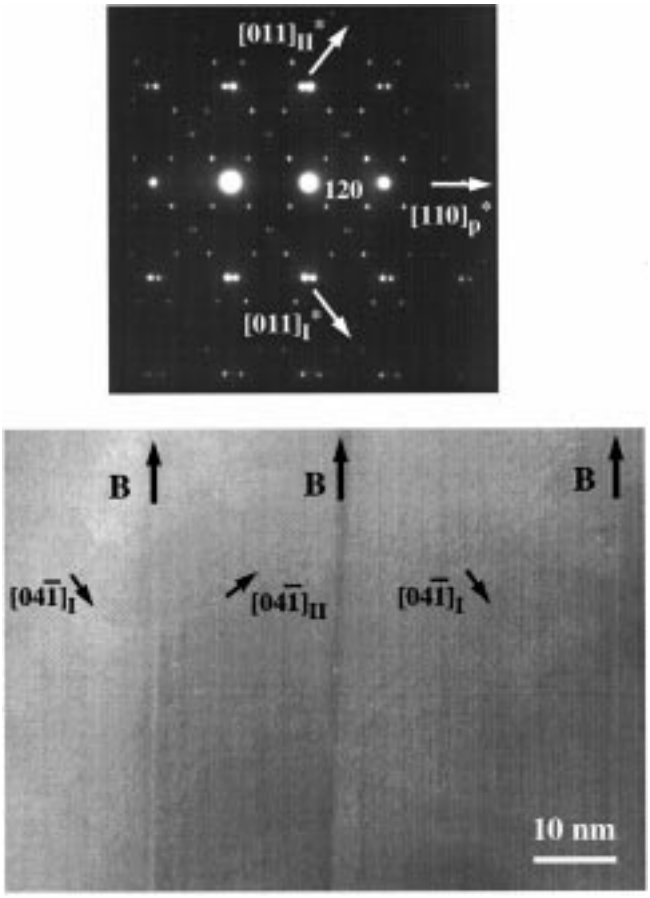

Figure 8. SAED pattern is characterisitic of the twinned microcrystal. Common reciprocal direction is [102]*. Low-resolution image shows planar domain boundaries parallel to (102).

manganese. The magnetic moments corresponding to four cations on equivalent positions are labeled as follows: $\vec{S}_1$ on 0, 0, z; $\vec{S}_2$ on 0, 0, $-z$; $\vec{S}_3$ on 0, $^1/_2$, $^1/_2 - z$; $\vec{S}_4$ on 0, $^1/_2$, $^1/_2 + z$.

The four base vectors which represent the possible magnetic modes of coupling are expressed according to Bertaut's notation: $\vec{F} = \vec{S}_1 + \vec{S}_2 + \vec{S}_3 + \vec{S}_4$; $\vec{G} = \vec{S}_1 - \vec{S}_2 + \vec{S}_3 - \vec{S}_4$; $\vec{C} = \vec{S}_1 + \vec{S}_2 - \vec{S}_3 - \vec{S}_4$; $\vec{A} = \vec{S}_1 - \vec{S}_2 - \vec{S}_3 + \vec{S}_4$.

Applying the projection operator method, we found the modes compatible with the eight irreducible representations (Table 4) allowed by the space group *Ammm*. For the propagation vector $\vec{k} = (^1/_2,0,0)$, we obtained the same eight one-dimensional real representations, due to the absence of translational symmetry element along x.[13]

Among the eight possible magnetic models, some representations can be discarded, considering the extinction rules applied to the magnetic structure factors: as pointed out, the Miller indices of all the reflections exhibit the $k + l = 2n + 1$ rule, which are characteristic of the G and C modes. Then only the configurations containing the G or C modes are in agreement with the selection rules. In addition, if we consider the magnetic interactions between d^4 cations, analysis of the superexchange path allows us to propose a magnetic structure model for $LaBaMn_2O_{5.5}$. Ferromagnetic interactions are

(13) Sivardière, J. CENG-CEA Internal report, 1968.

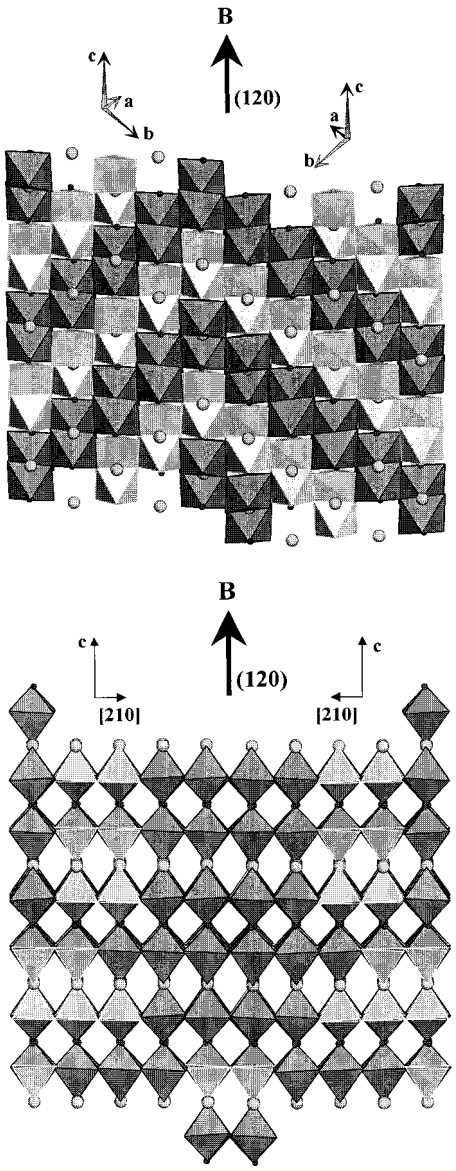

Figure 9. Proposed structural model: (a) direction of projection is identical to experimental image; (b) model has been rotated of 57° around [210].

expected when the empty $d_{x^2-y^2}$ orbital and the half-occupied d_{z^2} orbital are linked through the anionic ligand, while antiferromagnetic interactions occur when two empty $d_{x^2-y^2}$ orbitals are linked. These considerations allow a model for the magnetic structure to be proposed. The latter is based on the observed Jahn−Teller distortions and the superexchange rules. Along the $\vec{b}$ axis the d_{z^2} orbitals alternate with $d_{x^2-y^2}$ orbitals, which leads to ferromagnetic chains. Along $\vec{a}$, the $d_{x^2-y^2}$ orbitals give antiferromagnetic interactions, in agreement with the propagation vector $\vec{k} = (^1/_2,0,0)$. Along $\vec{c}$, we observe two different interactions: an antiferromagnetic coupling between $d_{x^2-y^2}$ orbitals of the $Mn_{(2)}$ cations and a ferromagnetic coupling between d_{z^2} orbital of $Mn_{(1)}$ and $d_{x^2-y^2}$ orbital of $Mn_{(2)}$ cations. These pictures are merely compatible with the G mode. Then only the Γ_3, Γ_4, and Γ_8 representations, which contain respectively the G_y, G_x, and G_z modes, are compatible with the experimental data. These three representations give rise to the same magnetic reflections, but their intensities are significantly different. The refinement of the mag-

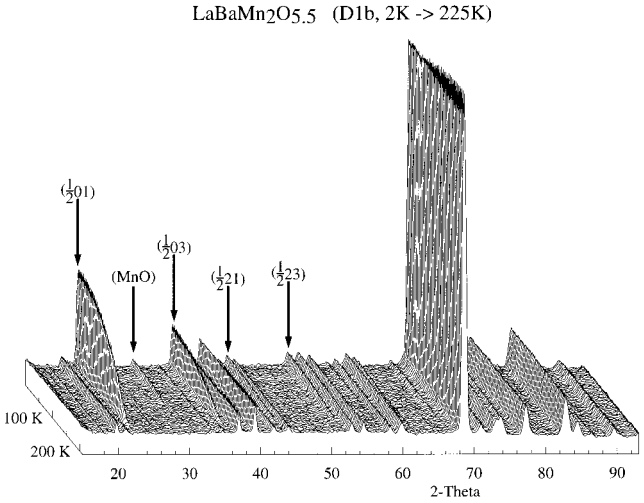

Figure 10. Thermal dependence of the neutron diffraction pattern in the temperature range 1.7−210 K. The magnetic reflections of $LaBaMn_2O_{5.5}$ are indexed in the chemical cell, and the main magnetic reflection of MnO is also indicated.

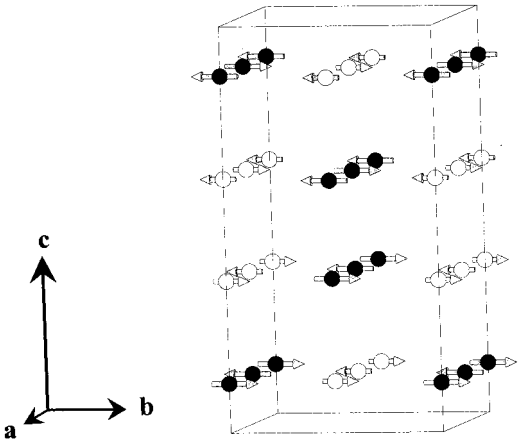

Figure 11. Magnetic structure of $LaBaMn_2O_{5.5}$. Manganese atoms in octahedral coordination are drawn in white; manganese in pyramidal coordination are in black. Arrows represent moments on the manganese ions. The diamagnetic ions are omitted for clarity.

Table 4. Irreducible Representations of Couplings Modes in Space Group *Ammm* ($\vec{k}$ = (0,0,0) and $\vec{k}$ = ($^1/_2$,0,0) for Manganese Sublattice)

$\Gamma_1(+++)$	C_x	$\Gamma_5(++-)$	$F_y\ C_z$
$\Gamma_2(+-+)$	$C_y\ F_z$	$\Gamma_6(+--)$	F_x
$\Gamma_3(-++)$	$G_y\ A_z$	$\Gamma_7(-+-)$	A_x
$\Gamma_4(--+)$	G_x	$\Gamma_8(---)$	$A_y\ G_z$

netic structure, at 1.7 K, gives the best result with the G_y mode. If an A_z component, which is also allowed by the Γ_3 representation, was also active, several reflections with $k + l = 2n$ would be also observed. Careful inspection in the neighboring of the $^1/_2$02 and $^1/_2$11 reflections did not reveal these reflections, which means that the A_z mode is not active. The final reliability factors, with the G_y mode, are $R_{wp} = 5.99\%$, $R_p = 7.9\%$, $R_i = 6.14\%$, $R_m = 10.6\%$, $\chi^2 = 2.33$. The structural parameters are given in Table 1, and the magnetic structure is shown on Figure 11.

Figure 12 shows that the magnetic structure of $LaBaMn_2O_{5.5}$ can be described by a network of parallel ferromagnetic spin-ladders: Each ferromagnetic spin-ladder lies along the $\vec{b}$ axis in the (100) plane and is connected antiferromagnetically along the $\vec{a}$ and $\vec{c}$ axis

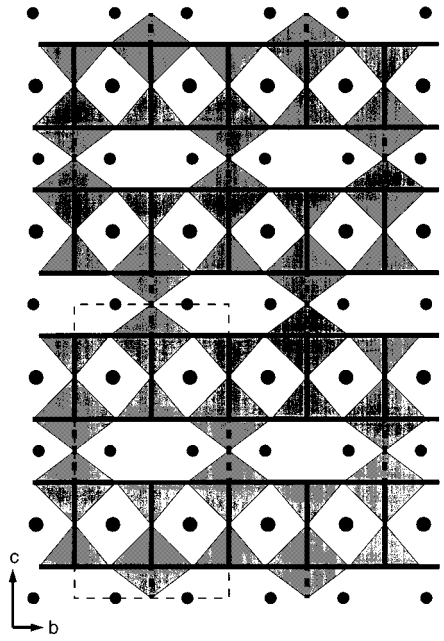

Figure 12. Superexchange pathways in $LaBaMn_2O_{5.5}$. The ferromagnetic pathways, drawn with thick lines, are arranged as ladders. The thick dotted lines show the antiferromagnetic pathway. The cell is drawn with the thin dotted line.

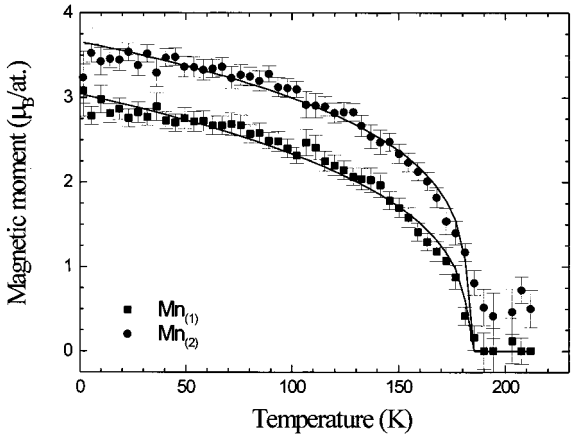

Figure 13. Magnetic moment as a function of temperature. The lines are fitted with a power law: $M = M_0(1 - T/T_c)^{2\beta}$.

to the neighboring ladders. In the (100) plane, half of the manganese ions of every ladder are connected to adjacent ladders by the $Mn_{(2)}-O-Mn_{(2)}$ antiferromagnetic pathway (dotted line on Figure 12). Along the [100] direction, all the manganese ions of a ladder are connected antiferromagnetically to the upper and lower ladders.

The refined values for the magnetic moments, from 1.5 to 220 K, are displayed in Figure 13. At $T = 1.5$ K, the magnetic moments of the two sites are 3.0(3) μ_B for $Mn_{(1)}$ and 3.4(3) μ_B for $Mn_{(2)}$. The magnetic moments are significantly reduced from their spin-only values (4 μ_B). This reduction is too large to be explained by covalency effects[14] but is commonly observed in oxygen-deficient perovskites.[7,8,15,16] This reduction might be

(14) Owen, J.; Thornley, J. H. M. *Reports on progress in Physics*; Stickland, A. C., Ed.; The Institute of Physics and Physical Society: London, 1966; Vol. XXIX, Part II.
(15) Caignaert, V. *J. Magn. Magn. Mater.* **1997**, *166*, 117.
(16) Battle, P. D.; Bollen, S. K.; Gibb, T. C.; Matsuo, M. *J. Solid State Chem.* **1991**, *90*, 42.

related to the occurrence of twinning, which induces misalignment of spin directions in the neighboring domain planes and hence to a small reduction in the average ordered component of the magnetic moments as measured in the neutron diffraction experiment.

5. Conclusion

This study has shown the possibility of stabilizing a new ordered oxygen-deficient perovskite, using a topotactic deoxygenation method. It suggests that other ordered oxygen-deficient perovskites may exist, provided the oxygen loss to be carefully controlled during the reduction process. The second important point concerns the existence of two different sites for manganese (octahedral and pyramidal) in this pure Mn^{3+} phase. This leads to an original antiferromagnetic structure, in which manganese spins form ferromagnetic spin-ladders along the $\vec{b}$ axis which are antiferromagnetically coupled along the $\vec{a}$ and $\vec{c}$ axis. The synthesis of other ordered oxygen-deficient members in this series should allow new magnetic structures and properties to be generated, in the future.

CM980469H